Materials Advances

ROYAL SOCIETY OF CHEMISTRY

PAPER

View Article Online
View Journal | View Issue

Cite this: *Mater. Adv.*, 2026, 7, 5361

Exploring structural, electronic, mechanical, and hydrogen storage properties of Mg_3ZH_8 (Z = Fe, Co): a density functional theory study

Md. Hasan Mia, *[a] Md. Zahid Hasan, [b] A. Arunkumar*[c] and S. AlFaify[d]

Received 13th March 2026,
Accepted 23rd April 2026

DOI: 10.1039/d6ma00353b

rsc.li/materials-advances

The development of efficient hydrogen storage materials is crucial for practical hydrogen energy utilization. This study uses first-principles density functional theory (DFT) to examine the structural, electronic, mechanical, optical, and hydrogen storage properties of Mg_3ZH_8 (Z = Fe, Co) complex hydrides. Both compounds are thermodynamically and dynamically stable, as confirmed by negative formation energies and phonon spectra free of imaginary modes. Mg_3FeH_8 exhibits a ferromagnetic metallic ground state, while Mg_3CoH_8 shows non-magnetic metallic behavior, with transition-metal d states playing a key role in their electronic and magnetic properties. The calculated gravimetric hydrogen storage capacities of 5.90 wt% for Mg_3FeH_8 and 5.76 wt% for Mg_3CoH_8, along with high volumetric densities of 195.6 and 186.6 g H_2 per L, respectively, surpass current U.S. Department of Energy targets. Dehydrogenation thermodynamics show moderate desorption temperatures, with Mg_3FeH_8 demonstrating better hydrogen release behavior. Mechanical analysis indicates ductility with positive Cauchy pressure, high Pugh's ratios, and moderate Vickers hardness, suggesting resistance to hydrogen embrittlement. Optical and transport properties reveal metallic conductivity, which enhances hydrogen desorption kinetics. These findings position Mg_3ZH_8 (Z = Fe, Co) as a promising hydrogen storage material and provide a solid theoretical basis for future experimental work.

1. Introduction

Hydrogen energy has come to light as a possible way to solve both the world's energy crisis and pollution problems. Hydrogen is a clean energy carrier that has a high gravimetric energy density and does not release any carbon when used. It is seen as a good replacement for traditional fossil fuels. The increasing demand for clean and sustainable energy has intensified interest in hydrogen as a promising energy carrier due to its high gravimetric energy density and environmentally benign combustion products.[1–3] Despite significant progress in hydrogen production and utilization technologies, the lack of safe, efficient, and reversible hydrogen storage materials operating under near-ambient conditions remains a major obstacle to the large-scale deployment of hydrogen-based energy systems. Among the available storage strategies, solid-state hydrogen storage using metal and complex hydrides is considered one of the most promising approaches because of its high volumetric density, enhanced safety, and compactness compared to compressed or liquefied hydrogen. To guide the development of practical hydrogen storage materials, the U.S. Department of Energy (DOE)[4] has established performance targets for onboard storage systems, including a gravimetric hydrogen capacity exceeding 5.5 wt%, a volumetric capacity above 40 g H_2 per L, operating temperatures in the range of 233–333 K, and moderate pressures below 10 MPa. Achieving these targets simultaneously remains challenging, as many known hydrides exhibit either excessively strong metal–hydrogen bonding that leads to high desorption temperatures or insufficient thermodynamic stability that compromises reversibility and cycling performance.

In recent years, complex and perovskite-type hydrides have emerged as an important class of hydrogen storage materials because their flexible crystal chemistry enables systematic tuning of structural, electronic, and thermodynamic properties. Numerous categories of complex hydrides, such as borohydrides, amides, and alanates, have undergone extensive research for hydrogen storage purposes. Alkali alanates $MAlH_4$

[a] *Department of Computer and Communication Engineering, International Islamic University Chittagong, Kumira, Chittagong 4318, Bangladesh. E-mail: mdhasan111.ru@gmail.com*
[b] *Materials Research and Simulation Lab, Department of Electrical and Electronic Engineering, International Islamic University Chittagong, Kumira, Chittagong 4318, Bangladesh*
[c] *Department of Condensed Matter Physics, Saveetha School of Engineering, Saveetha Institute of Medical and Technical Sciences, SIMATS, Chennai, Tamil Nadu-602105, India. E-mail: arunkumara.phys@gmail.com*
[d] *Department of Physics, College of Science, King Khalid University, Post Box 960, Abha 61421, AlQura'a, Saudi Arabia*

(M = Li, Na, K) have garnered significant attention owing to their relatively high hydrogen density and reversible hydrogen absorption/desorption characteristics.[5] First-principles investigations of $MgVH_6$ and $MgSiH_6$ have demonstrated chemical stability, pressure-dependent phase behaviour, and notable electronic properties, such as metallic characteristics and superconductivity under extreme conditions, underscoring the adaptability of hexahydride systems.[6,7] Concurrently, double perovskite hydrides have become attractive options for multipurpose uses. For example, $KNaMg_2F_{6-x}H_x$ and $KNaAe_2H_6$ (Ae = Be, Mg, Ca) show semiconducting behaviour with ultraviolet absorption capacity and favourable desorption temperatures.[8] Furthermore, large hydrogen capacities and favourable formation energetics have been anticipated for a number of hexahydrides, such as Q_2FeH_6 (Q = Mg, Ca, Sr),[9] Mg_2XH_6 (X = Cr, Mn),[10] A_2LiCuH_6 (A = Be, Mg, Ca, Sr),[11] $KNaX_2H_6$ (X = Mg, Ca, and X_2CaCdH_6 (X = Rb, Cs).[12] Similarly, indirect band gap semiconductors with the capacity to store hydrogen have been found as A_2BH_6 (A = K, Rb; B = Ge, Sn) hydrides.[13] Additionally, it has been demonstrated that compositional tweaking, such as lithium doping in Na-based perovskites, improves photocatalytic activity and optoelectronic response.[14] Numerous first-principles studies have demonstrated promising hydrogen storage performance in alkaline-earth hydrides systems. For example, DFT investigations of alkali and alkaline-earth hydrides, including $AMAlH_4$ (AM = Li, Na, K and Rb),[15] XNH_6 (X = Li, Na, K),[16] $NaXH_3$ (X = Be, Mg, Ca, Sr),[17] and $RbXH_3$ (X = Mg, Ca, Sr, Ba),[18] have reported high gravimetric hydrogen capacities and favorable formation energetics. These investigations also emphasize the critical role of lattice environment, electronic structure, and bonding characteristics in determining hydrogen stability and release behavior. First-principles studies of Mg_3XH_8 (X = Ca, Sc, Ti, V, Cr, Mn) hydrides have shown that transition-metal substitution strongly affects lattice stability, hydrogen binding strength, and mechanical behavior.[19] These modifications lead to favorable gravimetric hydrogen densities and moderate desorption temperatures.

Despite these advances, Mg_3ZH_8 (Z = Fe, Co) hydrides containing late transition metals such as Fe and Co have not yet been systematically explored. Compared with early transition metals, Fe and Co possess more localized d electrons, which can significantly modify magnetic behavior, electronic conductivity, bonding character, and metal–hydrogen interactions. Understanding how these factors affect hydrogen storage thermodynamics, kinetics, and mechanical durability is essential for expanding the design space of Mg-based complex hydrides. Moreover, experimental data for Mg_3ZH_8 (Z = Fe, Co) systems are currently unavailable, underscoring the need for reliable theoretical benchmarks. In this work, we present a comprehensive first-principles investigation of Mg_3ZH_8 (Z = Fe, Co) complex hydrides. Structural stability, electronic and magnetic properties, mechanical and thermophysical behavior, optical response, and hydrogen storage characteristics are systematically examined. Multiple dehydrogenation pathways are analyzed to evaluate reaction energetics and hydrogen desorption temperatures. By directly comparing Fe- and Co-based systems, the role of late transition-metal substitution in tailoring hydrogen storage performance is clarified. The present study provides the first detailed theoretical benchmark for Mg_3ZH_8 (Z = Fe, Co) hydrides and offers guidance for future experimental synthesis and optimization.

2. Computational details

The hydrogen storage properties, thermo-mechanical, optoelectronic, and magnetic nature of Mg_3ZH_8 (Z = Fe, Co) hydrides were investigated based on density functional theory (DFT) using the CASTEP code.[20] Vanderbilt ultrasoft pseudopotentials were employed to describe the interaction between valence electrons and ionic cores. The exchange–correlation energy was treated using the generalized gradient approximation (GGA) with the Perdew–Burke–Ernzerhof (PBE) functional.[21] Mg_3ZH_8 (Z = Fe, Co) hydrides crystallize in a cubic structure with space group $Pm\bar{3}m$ (no. 221), belonging to the $m\bar{3}m$ point group. In the optimized structures, the transition metal atom (Fe or Co) occupies the 1a Wyckoff position at (1/2, 1/2, 0). Mg atoms are located at the 3c site with fractional coordinates (0, 0, 0). H atoms occupy the 8g Wyckoff position at (0.243175, 0.243175, 0.756825). These atomic positions were fully relaxed during geometry optimization. The optimized lattice parameters were found to be $a = b = c = 4.09$ Å for Mg_3FeH_8 and 4.15 Å for Mg_3CoH_8, corresponding to unit cell volumes of 68.39 Å^3 and 71.68 Å^3, respectively as shown in Table 1. Geometry optimizations were performed using the BFGS minimization algorithm.[22] The convergence criteria were set to 5×10^{-6} eV per atom for total energy, 0.01 eV Å^{-1} for maximum ionic force, 5×10^{-4} Å for maximum atomic displacement, and 0.02 GPa for maximum stress. All calculations were carried out at 0 K and zero external pressure. A Monkhorst–Pack k-point mesh[23] of $6 \times 6 \times 6$ was used for Brillouin zone integration. The plane-wave cutoff energy was fixed at 630 eV. A smearing width of 0.5 eV was applied to improve electronic convergence. Elastic constants were evaluated to determine the mechanical properties. The elastic moduli of the polycrystalline systems were derived using the Voigt–Reuss–Hill approximation.[24,25] Electronic band structures

Table 1 The calculated geometry optimized data, formation enthalpy, and gravimetric properties of Mg_3ZH_8 (Z = Fe, Co) hydrides with previously reported similar type of hydrides

Compounds	$a = b = c$	V	ΔE_{for}	ρ(g H_2 per L)	$C_{wt\%}$	T_{des} (K)
Mg_3FeH_8	4.09	68.39	−0.264	195.6	5.90	194.74
Mg_3CoH_8	4.15	71.68	−0.220	186.6	5.76	162.57
Mg_3ScH_8 (ref. 19)	4.73	—	−0.240	197	6.36	
Mg_3TiH_8 (ref. 19)	4.61	—	−0.250	218	6.21	
Mg_3VH_8 (ref. 19)	4.54	—	−0.230	234	6.07	
Mg_3CaH_8 (ref. 19)	4.90	—	−0.100	171	6.61	
Mg_3CrH_8 (ref. 19)	4.50	—	−0.280	242	6.02	
Mg_3MnH_8 (ref. 19)	4.47	—	−0.190	252	5.89	
Mg_3MnH_7 (ref. 26)	—	—	—	—	$5.2^{expt.}$	$530–640^{expt.}$
Mg_2FeH_6 (ref. 27)	—	—	—	—	$5.5^{expt.}$	$603^{expt.}$
MgH_2 (ref. 28)	—	—	—	—	$7.1^{expt.}$	$623–673^{expt.}$

and optical properties were calculated in reciprocal space using fully optimized crystal geometries. Optical properties were obtained within the CASTEP code through evaluation of the complex dielectric function. Phonon dispersion calculations for Mg_3ZH_8 (Z = Fe, Co) were performed using the finite-displacement method with ultrasoft pseudopotentials. A 4 × 4 × 4 Monkhorst–Pack *k*-point mesh was employed to ensure accurate force-constant determination and phonon convergence. Plane-wave energy cutoffs of 850 eV for Mg_3FeH_8 and 950 eV for Mg_3CoH_8 were used, and all computational parameters were carefully tested to obtain converged phonon spectra without imaginary frequencies.

3. Results and discussion

3.1 Phase stability and gravimetric properties

The optimized crystal structures and dynamical stability profiles of the Mg-based hydrides Mg_3ZH_8 (Z = Fe, Co) are shown in Fig. 1(a)–(c). Both compounds crystallize in a highly hydrogen-rich framework, where the choice of transition-metal cation at the Z site plays a decisive role in determining lattice geometry and stability. Table 1 summarizes the optimized structural parameters, volumetric and gravimetric hydrogen storage capacities of Mg_3ZH_8 (Z = Fe, Co) in comparison with previously reported Mg_3ZH_8-type hydrides. The calculated lattice parameters for Mg_3FeH_8 (a = 4.09 Å) and Mg_3CoH_8 (a = 4.15 Å) are smaller than those of Mg_3ScH_8, Mg_3TiH_8, and Mg_3CaH_8, reflecting the reduced atomic radii of Fe and Co and the resulting lattice contraction.[19] This compact crystal structure directly contributes to enhanced volumetric hydrogen storage performance.

Thermodynamic stability was evaluated by calculating the formation enthalpy (ΔE_f), defined as,

$$\Delta E_f = \frac{E_{tot}(Mg_3ZH_8) - 3E_{tot}(Mg) - E_{tot}(Z) - 4E_{tot}(H_2)}{N},$$

where $E_{tot}(Mg_3ZH_8)$ is the total energy of the optimized unit cell, $E_{tot}(Mg)$ and $E_{tot}(Z)$ are the energies of elemental Mg and Z (Fe or Co) in their stable crystalline phases, $E_{tot}(H_2)$ is the total energy of the hydrogen molecule, and N is the number of atoms per formula unit. The negative formation energies of Mg_3FeH_8 (−0.264 eV per atom) and Mg_3CoH_8 (−0.220 eV per atom) confirm their thermodynamic stability and are comparable to, or more favorable than, those reported for[19] Mg_3ScH_8, Mg_3TiH_8, Mg_3VH_8, and Mg_3MnH_8. Notably, Mg_3FeH_8 exhibits a formation energy close to that of Mg_3CrH_8, indicating similarly strong metal–hydrogen bonding, while maintaining a smaller lattice parameter. At present, no experimental data are available for these compounds; therefore, the present results provide the first systematic theoretical benchmark for this class of materials and offer valuable guidance for future experimental synthesis and characterization.

Dynamical stability was further assessed through phonon dispersion calculations, as shown in Fig. 1(a) and (b). The phonon characteristics reveal how hydrogen-rich stoichiometry and metal–hydrogen bonding collectively stabilize the lattice while enabling high gravimetric hydrogen capacity. The phonon spectra of both hydrides exhibit three acoustic branches and multiple optical modes, with no imaginary frequencies observed throughout the Brillouin zone. This confirms that Mg_3ZH_8 (Z = Fe, Co) are dynamically stable and free from lattice instabilities. The optical phonon modes at higher frequencies are dominated by hydrogen vibrations, reflecting the strong metal–hydrogen bonding and hydrogen-rich nature of the lattice. A pronounced frequency gap between acoustic and optical phonon branches is observed in both compounds. This gap originates from the large mass contrast between light hydrogen atoms and heavier metal atoms (Mg and Z), which leads to well-separated low-frequency lattice translations and high-frequency hydrogen-dominated vibrations. The wider acoustic–optical gap observed in Mg_3FeH_8 compared to Mg_3CoH_8 reflects stronger Fe–H bonding and a stiffer local hydrogen environment, consistent with its more negative formation energy and higher lattice rigidity.

The *ab initio* molecular dynamics (AIMD) simulations for Mg_3FeH_8 and Mg_3CoH_8 were performed using a 2 × 2 × 2 supercell with a timestep of 1 fs in the NVT ensemble at 300 K, after an initial equilibration phase. The simulations ran for 5000 fs, providing sufficient sampling of the atomic dynamics. The Fig. 2(a) and (b) show the temperature evolution of both hydrides during the simulations, with the temperature fluctuating around 300 K. The temperature was analyzed using the kinetic energy relation: $T = \frac{2E_{kin}}{3Nk_B}$; where E_{kin} is the average kinetic energy, N is the number of atoms, and k_B is Boltzmann's constant. In these simulations, the temperature fluctuations

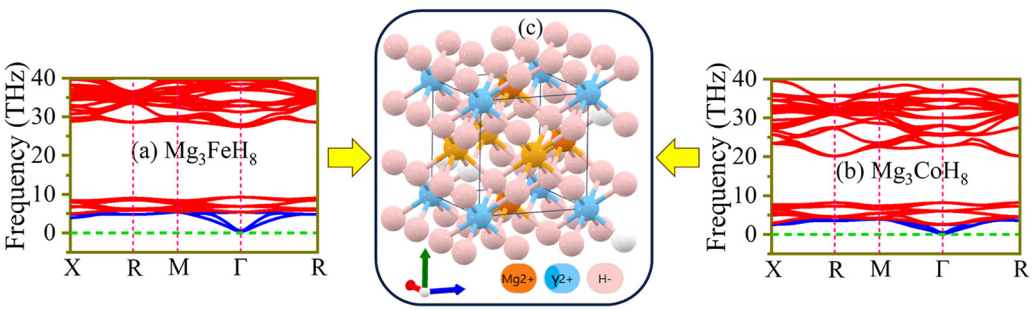

Fig. 1 (a)–(c) The phonon dispersion with three-dimensional structure of Mg based Mg_3ZH_8 (Z = Fe, Co) hydrides.

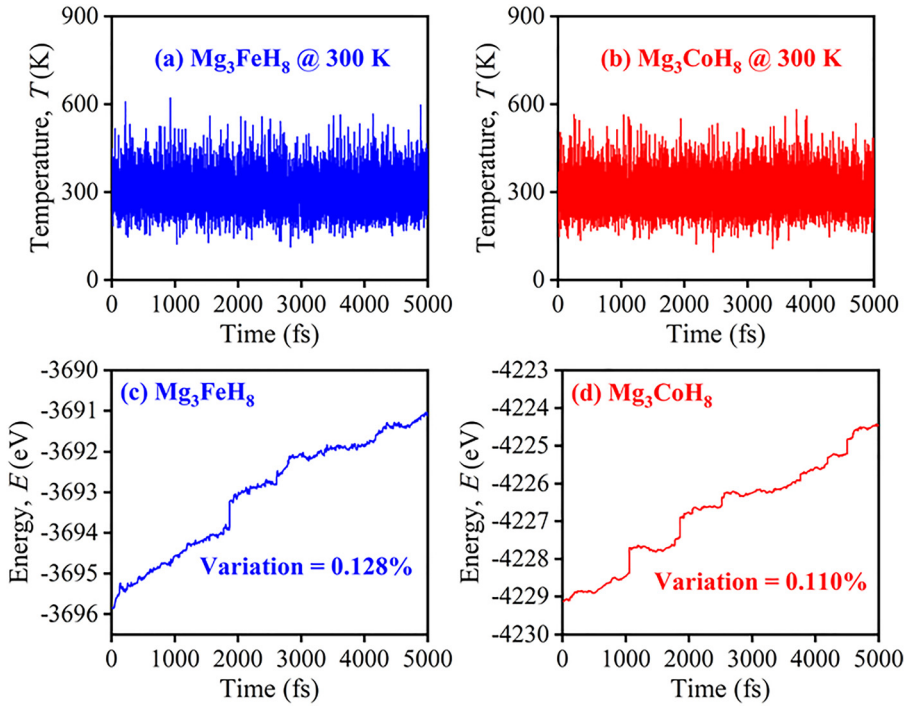

Fig. 2 (a)–(d) Temperature and energy evolution of Mg_3FeH_8 and Mg_3CoH_8 at 300 K over 5000 fs. Temperature remains stable around 300 K, while total energy shows slight drifts with variations of 0.128% and 0.110%, respectively.

around 300 K indicate dynamic stability for both hydrides, as neither system exhibits significant deviations from the target temperature. The stable behavior of the temperature profiles suggests that both Mg_3FeH_8 and Mg_3CoH_8 maintain their structural integrity and dynamic stability at room temperature, making them suitable candidates for hydrogen storage applications under practical conditions. The time evolution of the total energy for Mg_3FeH_8 and Mg_3CoH_8 systems is presented in Fig. 2(c) and (d). In both cases, the energy exhibits a slight upward drift over the simulation time of 5000 fs. For Mg_3FeH_8, the energy increases from −3695.85376 eV to −3691.13808 eV, corresponding to a relative variation of approximately 0.128%. Similarly, Mg_3CoH_8 shows an increase from −4229.13344 eV to −4224.47209 eV, yielding a relative variation of about 0.110%. Despite these small increases, the overall fluctuations remain minimal compared to the total energy scale, indicating good stability of the simulations. The slightly lower variation observed in Mg_3CoH_8 suggests marginally improved energy conservation compared to Mg_3FeH_8.

In this study, the hydrogen storage potential of Mg_3ZH_8 (Z = Fe, Co) hydrides was evaluated by calculating the gravimetric hydrogen capacity using,[29]

$$C_{wt\%} = \frac{(H/M)m_H}{m_{host} + (H/M)m_H} \times 100,$$

where H/M is the hydrogen-to-metal ratio, m_H is the atomic mass of hydrogen, and m_{host} is the mass of the host lattice. Owing to their hydrogen-rich stoichiometry (eight hydrogen atoms per formula unit) and the low atomic mass of magnesium, Mg_3ZH_8 (Z = Fe, Co) hydrides exhibit high gravimetric capacities of 5.89 wt% for Mg_3FeH_8 and 5.76 wt% for Mg_3CoH_8 are shown in Fig. 3(a). The small difference in gravimetric capacity between Mg_3FeH_8 and Mg_3CoH_8 reflects the subtle mass and bonding variations between Fe and Co, indicating that Z-site substitution provides an effective route to tune hydrogen density without degrading phase or dynamical stability. Notably, the gravimetric hydrogen storage capacities of Mg_3FeH_8 and Mg_3CoH_8 exceed the U.S. DOE near-term gravimetric target of 5.5 wt%, highlighting their promise for practical solid-state hydrogen storage applications.[30] The gravimetric hydrogen storage capacities of Mg_3FeH_8 (5.90 wt%) and Mg_3CoH_8 (5.76 wt%) fall within the typical range reported for Mg_3ZH_8-type hydrides[19] in Table 1. Additionally, the calculated values of $C_{wt\%}$ for both hydrides are in good agreement with the experimental values reported for other hydrides, as outlined in Table 1, confirming the reliability of our theoretical predictions.

Since there are no previously reported experimental or theoretical gravimetric hydrogen storage capacities for Mg_3ZH_8 (Z = Fe, Co), Fig. 3(b) presents a comparative analysis with a range of well-established complex hydrides. Both Mg_3FeH_8 and Mg_3CoH_8 exhibit among the highest gravimetric hydrogen storage capacities, surpassing or closely matching widely studied Mg-based complex hydrides such as Mg_2NiH_6 (5.32 wt%),[31] Mg_2CoH_6 (5.29 wt%),[31] Mg_2CrH_6 (5.60 wt%),[10] and Mg_2VH_6 (5.72 wt%).[32] Their performance also exceeds that of several alkali- and alkaline-earth-stabilized hydrides, including, Mn_3NaH_8 (4.12 wt%),[33] Mn_3KH_8 (3.80 wt%),[33] K_2LiAlH_6 (5.08 wt%),[34] Ca_2VH_6 (4.41 wt%),[32] Rb_2NaGaH_6 (1.48 wt%),[35] and $KNaMg_2H_6$ (5.19 wt%).[8] This comparison demonstrates that Mg_3ZH_8 (Z = Fe, Co) hydrides combine high hydrogen

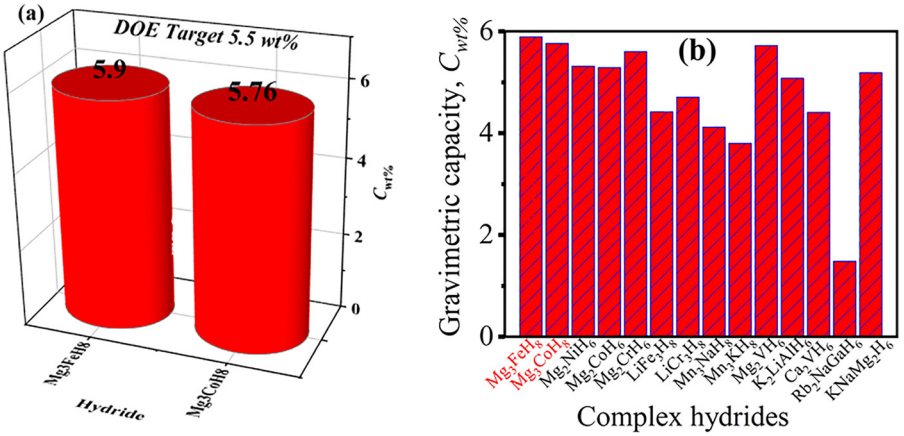

Fig. 3 (a) Gravimetric capacity of Mg_3ZH_8 (Z = Fe, Co), and (b) comparison of gravimetric hydrogen storage capacities of Mg_3ZH_8 (Z = Fe, Co) with previously reported complex hydrides.

content with a lightweight Mg-based framework, positioning them among the most competitive solid-state hydrogen storage materials reported to date and underscoring their scientific relevance and potential for practical hydrogen energy applications. Our study aims to provide foundational insights into the hydrogen storage capacities of Mg_3FeH_8 and Mg_3CoH_8 at the material level. System-level performance would require experimental validation and simulations that account for the integration of these materials into practical storage systems, which is a necessary next step in future research.

In addition to gravimetric hydrogen storage capacity, the volumetric hydrogen storage capacity (ρ_{vol}) is a critical parameter for evaluating the practical applicability of solid-state hydrogen storage materials, particularly for space-constrained applications such as onboard storage systems. The volumetric capacity quantifies the amount of hydrogen that can be stored per unit volume of the material and is expressed in g H_2 per L. Following the methodology adopted in the referenced hydrogen-storage studies, the volumetric hydrogen storage capacity is calculated using the relation:[29]

$$\rho_{vol} = \frac{N_H \cdot m_H}{V(L) \cdot N_A},$$

where N_H is the total number of hydrogen atoms contained within the crystallographic unit cell, m_H is the molar mass of hydrogen (1.008 g mol^{-1}, V is the unit-cell volume expressed in liters, and N_A is Avogadro's number. The unit-cell volume is obtained directly from the optimized lattice parameters, ensuring that the calculated ρ_{vol} reflects the intrinsic structural compactness of the hydride. Table 1 indicates that the calculated volumetric hydrogen storage capacities of Mg_3FeH_8 and Mg_3CoH_8 are 195.6 and 186.6 g H_2 per L, respectively, which are comparable to those of Mg_3ScH_8 (197 g H_2 per L) and higher than that of Mg_3CaH_8 (171 g H_2 per L).[19] Although lower than the high volumetric capacities reported for Mg_3TiH_8, Mg_3VH_8, Mg_3CrH_8, and Mg_3MnH_8, both compounds far exceed the U.S. DOE volumetric hydrogen storage target of ~40 g H_2 per L.[19] These results indicate that Mg_3FeH_8 and Mg_3CoH_8 achieve a favorable balance between structural compactness and hydrogen storage efficiency within the Mg_3ZH_8 hydride family.

A key parameter for hydrogen storage applications is the hydrogen desorption temperature, T_{des}, which defines the thermal conditions required for hydrogen release. Following the approach proposed by Ikeda *et al.*,[36] the hydrogen decomposition reaction for Mg_3ZH_8 (Z = Fe, Co) hydrides is expressed as: $Mg_3ZH_8 \rightarrow 3Mg + Z + 4H_2$.

Based on this reaction, the hydrogen decomposition enthalpy (ΔH) is calculated as:

$$\Delta H = 3H_{Mg} + H_Z + 4H_{H_2} - H_{Mg_3ZH_8}$$

where $H_{Mg_3ZH_8}$ represents the enthalpy of the corresponding system. The enthalpy is determined by:

$$H = E_{ele} + E_{ZPE}$$

where E_{ele} and E_{ZPE} denote the electronic total energy and the zero-point energy, respectively. The zero-point energy is estimated from the phonon density of states as:

$$E_{ZPE} = \frac{\int h\omega g(\omega) d\omega}{2}.$$

where h, ω, and $g(\omega)$ are Planck's constant, phonon frequency, and phonon density of states, respectively.

The hydrogen desorption temperature (T_{des}) is estimated using:

$$T_{des} = -\frac{\Delta H}{\Delta S}.$$

where, ΔH is the decomposition enthalpy and ΔS is the entropy change of the reaction. In this work, ΔS is approximated as the entropy of hydrogen gas (130.7 J mol^{-1} K^{-1}).[8,31–35] Using this thermodynamic framework, the desorption temperatures for Mg_3FeH_8 and Mg_3CoH_8 were calculated to be 194.74 K and 162.57 K, respectively. These values suggest moderate hydrogen desorption behavior for both materials under practical conditions. The calculated T_{des} values for both hydrides are lower than the experimental values for other hydrides reported in

Table 1. The relatively low desorption temperatures indicate that hydrogen release can occur at mild temperatures, which helps to reduce thermal stress during hydrogen absorption and desorption cycles. From a durability perspective, these moderate desorption temperatures imply balanced thermodynamic stability, enabling reversible hydrogen absorption and release without excessive heating that could lead to lattice degradation or phase segregation. Although the predicted T_{des} for both hydrides are slightly below the U.S. DOE target window of 233–333 K, the results indicate a favorable balance between stability and hydrogen release under near-ambient conditions.

The hydrogen diffusion behavior in Mg_3FeH_8 and Mg_3CoH_8 is analyzed using the activation energy profiles shown in Fig. 4(a) and (b). In hydrogen storage materials, atomic migration is governed by the activation energy barrier, where lower values facilitate easier hydrogen transport and improved absorption/desorption kinetics. The diffusion pathways were evaluated using the nudged elastic band (NEB) method, which determines the minimum energy path and corresponding barriers.[37] Two possible diffusion pathways (path 1 and path 2) are considered for both compounds. For Mg_3FeH_8, the activation energies are 0.45 eV for path 1 and 1.69 eV for path 2, indicating that hydrogen migration is more favorable along path 1. In contrast, Mg_3CoH_8 exhibits lower barriers of 0.20 eV for path 1 and 1.39 eV for path 2, suggesting enhanced hydrogen mobility compared to Mg_3FeH_8. The relatively low activation energy along the preferred pathway, particularly in Mg_3CoH_8, indicates efficient hydrogen diffusion within the lattice. Overall, these results confirm that hydrogen transport is not kinetically hindered and support the suitability of these materials for hydrogen storage applications.

3.2 Electronic properties

Hydrogen absorption and desorption kinetics in solid-state hydrides are strongly influenced by their electronic structure, as the availability of electronic states near the Fermi level governs charge transfer, metal–hydrogen bonding, and hydrogen diffusion processes. Perovskite and complex hydrides have therefore attracted significant attention as promising hydrogen storage materials. In this section, the electronic properties of Mg_3ZH_8 (Z = Fe, Co) complex hydrides are investigated through a detailed analysis of their electronic band structures, total density of states (TDOS), and partial density of states (PDOS).

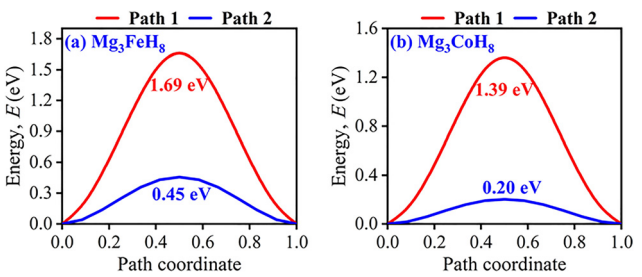

Fig. 4 Hydrogen diffusion energy profiles for (a) Mg_3FeH_8 and (b) Mg_3CoH_8 along two possible migration pathways (path 1 and path 2) calculated using the NEB method.

Fig. 5(a) and 6(a) display the calculated electronic band structures of Mg_3FeH_8 and Mg_3CoH_8, where the horizontal dashed line represents the Fermi level (E_F). The band structures were obtained within the GGA-PBE framework over an energy window from −6.0 to 6.0 eV, with E_F set to 0 eV. The Kohn–Sham eigenvalues were plotted along the high-symmetry directions X–R–M–Γ–R of the first Brillouin zone. Both Mg_3FeH_8 and Mg_3CoH_8 exhibit multiple electronic bands crossing the Fermi level, indicating the absence of a band gap and confirming their metallic ground state. The band dispersion near E_F provides further insight into their electronic transport behavior. Several bands crossing E_F display steep slopes along specific high-symmetry directions, reflecting strong orbital overlap and enhanced electronic delocalization. Mg_3FeH_8 shows relatively steeper band curvature near E_F compared to Mg_3CoH_8, suggesting a smaller carrier effective mass and higher carrier mobility. This behavior is primarily attributed to stronger Fe (3d)–H (1s) hybridization, whereas Mg_3CoH_8 exhibits slightly flatter bands due to comparatively weaker Co-3d contributions.

The steep dispersion of electronic bands near E_F implies a reduced carrier effective mass and, consequently, a higher Fermi velocity, given by[38,39]

$$v_F = \sqrt{\frac{E_F}{m^*}},$$

where m^* is the carrier effective mass. A higher Fermi velocity corresponds to enhanced carrier mobility and improved electrical and thermal transport. In this regard, Mg_3FeH_8 is expected to exhibit superior electronic transport properties compared to Mg_3CoH_8, consistent with its higher TDOS and stronger d-orbital participation near E_F. The metallic behavior of Mg_3ZH_8 (Z = Fe, Co) can also be assessed using the metallic fraction,[38,39]

$$f_m = \frac{n_m}{n_e} = \frac{k_B T \times N(E_F)}{n_e},$$

where n_m is the number of thermally excited electrons, n_e is the total number of valence electrons, and $N(E_F)$ is the TDOS at the

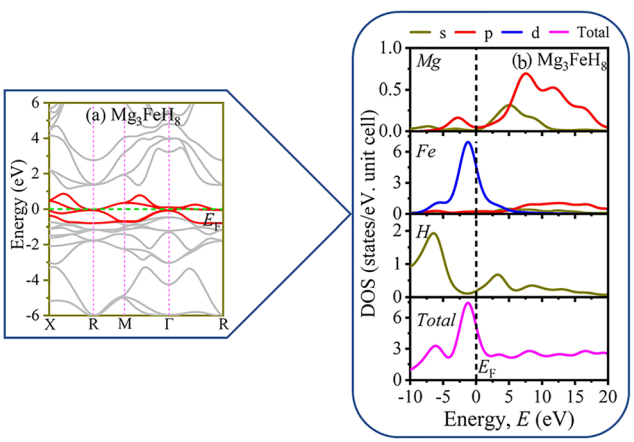

Fig. 5 (a) and (b) The electronic band structure with partial and total density of states of Mg_3FeH_8 complex hydride.

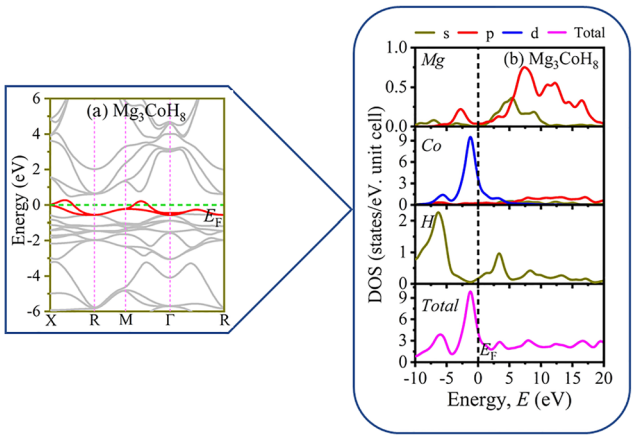

Fig. 6 (a) and (b) The electronic band structure with partial and total density of states of Mg_3CoH_8 complex hydride.

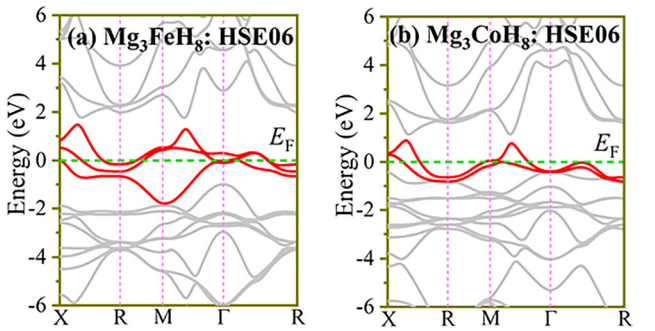

Fig. 7 Electronic band structures of (a) Mg_3FeH_8 and (b) Mg_3CoH_8 calculated using the HSE06 hybrid functional. The Fermi level is set at 0 eV (green dashed line).

Fermi level. The calculated values of f_m for Mg_3ZH_8 (Z = Fe, Co) are shown in Table 2. Since, f_m is directly proportional to $N(E_F)$, Mg_3FeH_8 exhibits a higher metallic fraction at room temperature than Mg_3CoH_8, implying a larger population of mobile charge carriers. The metallic conductivity, enhanced carrier mobility, and appreciable metallic fraction of Mg_3ZH_8 (Z = Fe, Co) hydrides have important implications for hydrogen storage applications. Metallic electronic behavior facilitates efficient charge transfer and heat dissipation during hydrogen absorption and desorption cycles, reducing kinetic barriers and localized thermal buildup.

Fig. 5(b) and 6(b) display the partial and total density of states of Mg_3FeH_8 and Mg_3CoH_8 hydrides. The total and partial density of states (TDOS and PDOS) of Mg_3ZH_8 (Z = Fe, Co) clarify the orbital contributions governing the valence and conduction regions. For both Mg_3FeH_8 and Mg_3CoH_8, the TDOS shows a finite value at the Fermi level, confirming their metallic nature. States near E_F are dominated by transition-metal d orbitals, with Fe-3d states contributing most strongly in Mg_3FeH_8 and Co-3d states in Mg_3CoH_8. This dominant d-state presence explains the band crossings at E_F and the high carrier density. In the valence band region, extending from about −6 eV up to the Fermi level, the DOS is mainly composed of hybridized metal d and hydrogen 1s states, indicating strong metal–hydrogen bonding. The sharp d-orbital peaks just below E_F reflect localized d electrons, while the broader H-1s contribution at lower energies signifies covalent interaction with the metal framework. Magnesium s and p states contribute weakly in this region, acting mainly as a charge donor to the metal–hydrogen network. In the conduction band region above E_F, the DOS is again dominated by metal d states with minor contributions from Mg-p orbitals, indicating that electronic transport is primarily governed by the transition-metal sublattice. The similarity in DOS distribution for Fe- and Co-based systems suggests that Z-site substitution mainly tunes the intensity and energy position of d-state peaks rather than altering the overall electronic character. This d-H hybridization near the Fermi level is crucial for metallic conductivity and supports efficient charge transfer and lattice screening, which are favorable for hydrogen diffusion and desorption kinetics.

Further, the electronic band structures of Mg_3FeH_8 and Mg_3CoH_8 were calculated using the HSE06 functional. As shown in Fig. 7(a) and (b), both compounds exhibit metallic behavior. This is confirmed by the presence of several energy bands crossing the Fermi level. This indicates the absence of a band gap and confirms the availability of free charge carriers in both systems. In Mg_3FeH_8, the bands near the Fermi level show relatively stronger dispersion compared to Mg_3CoH_8, suggesting enhanced electronic conductivity due to more pronounced hybridization between Fe 3d-states and H 1s-states. In contrast, Mg_3CoH_8 displays slightly flatter bands in certain regions, indicating comparatively localized electronic states. The overall metallic nature of both compounds is beneficial for hydrogen storage applications, as it promotes efficient charge transfer and heat dissipation, which are essential for improving hydrogen absorption and desorption kinetics.

3.3 Magnetic properties

To clarify the magnetic characteristics of Mg_3ZH_8 (Z = Fe, Co), spin-polarized electronic band structure calculations were performed within the PBE–GGA framework, as presented in Fig. 8(a) and (b). The band structures are resolved into spin-up (red) and spin-down (blue) channels. Fig. 8(a) shows the spin-polarized electronic band structure of Mg_3FeH_8, where a pronounced asymmetry between the spin-up and spin-down bands is observed near the Fermi level. Several Fe-derived bands cross E_F in only one spin channel, indicating strong

Table 2 Comparative metallicity, metallic fraction, and orbital character for Mg_3ZH_8 (Z = Fe, Co)

Compound	TDOS at E_F (states per eV)	Metallic fraction f_m (300 K)	Metallic strength	Dominant orbital at E_F
Mg_3FeH_8	~5.43	$\sim 7.3 \times 10^{-3}$	Strong metallic	Fe-3d with H-1s hybridization
Mg_3CoH_8	~3.91	$\sim 4.4 \times 10^{-3}$	Moderate metallic	Co-3d with H-1s contribution

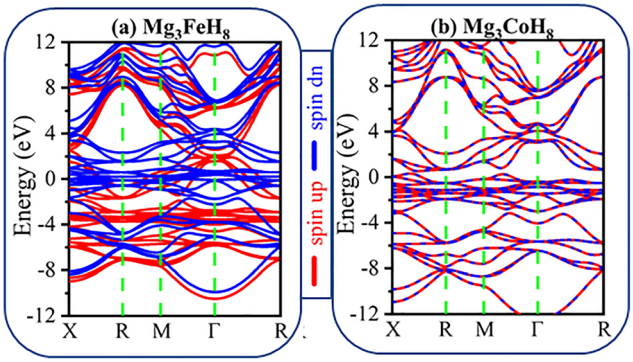

Fig. 8 (a) and (b) The spin polarized electronic band structure of Mg_3ZH_8 (Z = Fe, Co) hydride.

exchange splitting of the Fe 3d states. This spin-dependent band dispersion leads to unequal occupation of the two spin channels and results in a finite net magnetic moment, confirming the ferromagnetic ground state of Mg_3FeH_8. The presence of magnetism in Mg_3FeH_8 is associated with stronger Fe–H hybridization, which can influence hydrogen bonding strength and thermodynamic stability. In contrast, the spin-polarized band structure of Mg_3CoH_8 in Fig. 8(b) exhibits nearly identical spin-up and spin-down bands throughout the Brillouin zone. No exchange splitting is observed at the Fermi level, and both spin channels show the same band crossings. This spin degeneracy indicates zero net spin polarization, confirming that Mg_3CoH_8 adopts a non-magnetic ground state.

Fig. 9(a)–(c) shows the spin-polarized PDOS of Mg_3FeH_8 hydride. A clear asymmetry between the spin-up and spin-down channels is observed, most prominently in the Fe-3d states near the Fermi level (E_F). This exchange splitting leads to unequal occupation of the two spin channels and gives rise to a finite net magnetic moment, confirming the ferromagnetic nature of the compound. The Mg-s and p states exhibit nearly symmetric spin-up and spin-down distributions around the Fermi level, indicating a negligible contribution to the magnetic moment and a primarily ionic role. In contrast, the Fe-s and p states exhibit clear spin asymmetry near E_F, induced by exchange splitting from Fe-d orbitals, confirming the ferromagnetic nature of the compound. The H-s states display weak induced spin polarization due to Fe–H hybridization, reflecting an indirect contribution to the overall ferromagnetic ground state. Fig. 10(a)–(c) presents the spin-polarized PDOS of Mg_3CoH_8. The spin-up and spin-down components of the Mg (s, p), Co (s, p, d), and H (s) orbitals are nearly identical across the entire energy range, and no noticeable exchange splitting is observed at the Fermi level (E_F). This spin symmetry results in zero net spin polarization, confirming that Mg_3CoH_8 adopts a non-magnetic ground state, in agreement with the spin-polarized band structure shown in Fig. 8(b). The absence of magnetism can be attributed to the nearly filled and weakly spin-polarized Co-3d states, which are insufficient to support exchange-driven magnetic ordering.

The presence of ferromagnetism in Mg_3FeH_8 is associated with stronger Fe–H hybridization and enhanced bonding anisotropy, which can influence hydrogen stability, whereas the non-magnetic character of Mg_3CoH_8 reflects more uniform Co–H bonding and comparatively weaker exchange-driven stabilization.

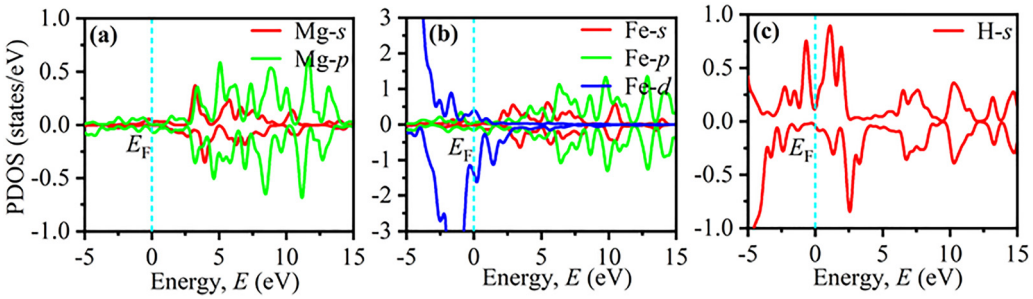

Fig. 9 (a)–(c) The spin polarized density of states of Mg_3FeH_8 complex hydride.

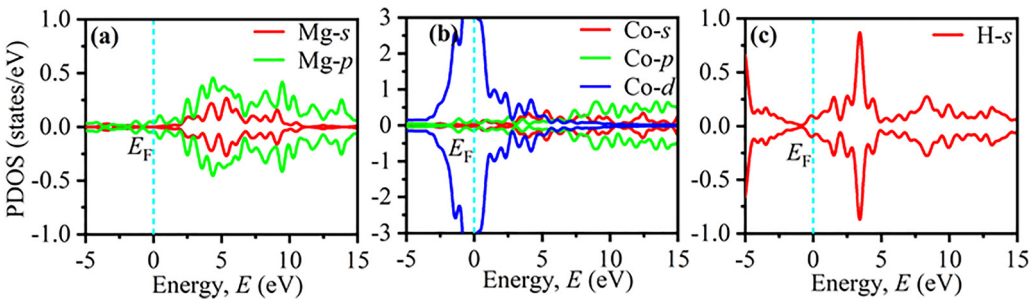

Fig. 10 (a)–(c) The spin polarized density of states of Mg_3CoH_8 complex hydride.

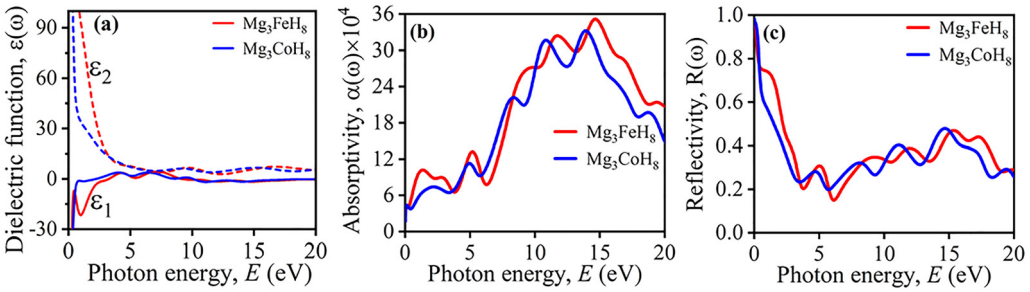

Fig. 11 Optical properties of Mg_3ZH_8 (Z = Fe, Co): (a) dielectric function, (b) absorption coefficient, and (c) reflectivity as a function of photon energy.

3.4 Optical properties

The optical response of Mg_3ZH_8 (Z = Fe, Co) hydrides provides insight into their electronic behavior and its relevance to hydrogen storage. The dielectric function,[40] $\varepsilon(\omega) = \varepsilon_1(\omega) + i\varepsilon_2(\omega)$, reveals strongly negative $\varepsilon_1(\omega)$ at low photon energies, confirming Drude-like metallic behavior and efficient free-carrier screening (Fig. 11(a)). This facilitates rapid charge redistribution and heat dissipation during hydrogen absorption–desorption cycles. Mg_3FeH_8 exhibits a slightly stronger response than Mg_3CoH_8, consistent with enhanced carrier mobility and stronger d-H hybridization. The large $\varepsilon_2(\omega)$ values in the low-energy region indicate strong absorption arising from interband transitions between transition-metal d states and H-1s orbitals (Fig. 11(a)). The absorption spectra further show strong absorptivity across the UV-visible range, with Mg_3FeH_8 displaying slightly higher absorption (Fig. 11(b)). The presence of absorption from low photon energies reflects efficient electronic excitations that support charge transfer and improve hydrogen desorption kinetics. Prominent UV peaks ($\sim$5 eV) originate from valence–conduction band transitions, indicating active electronic participation in hydrogen-related processes. The optical conductivity confirms metallic transport behavior, with high $\sigma_1(\omega)$ values indicating efficient charge transport and enhanced carrier dynamics (Fig. S1). The dispersive $\sigma_2(\omega)$ behavior reflects strong carrier screening, characteristic of metallic systems (Fig. S1). These features are beneficial for facilitating hydrogen diffusion and improving reversibility during cycling. High reflectivity at low energies further supports the metallic nature and strong free-carrier response (Fig. 11(c)). Its decrease at higher energies corresponds to interband transitions, consistent with the absorption behavior. The refractive index $n(\omega)$ and extinction coefficient $k(\omega)$ of Mg_3FeH_8 and Mg_3CoH_8 indicate strong light–matter interaction and metallic behavior (Fig. S2). High $n(\omega)$ at low energies and finite $k(\omega)$ confirm efficient charge transfer, supporting hydrogen desorption kinetics. The increase of $k(\omega)$ in the visible region reflects enhanced absorption and improved heat management during hydrogen cycling. Overall, the combined dielectric, absorption, conductivity, and refractive index responses confirm strong electronic activity and metallic behavior in Mg_3ZH_8 (Z = Fe, Co), which promote efficient charge transfer, thermal transport, and hydrogen desorption kinetics. These features reinforce the suitability of both hydrides for stable and efficient hydrogen storage.

3.5 Thermo-mechanical and anisotropic nature

Elastic constants provide fundamental insight into the mechanical stability, lattice rigidity, and hydrogen accommodation capability of solid-state hydrogen storage materials. In hydrogen-rich hydrides, appropriate elastic behavior is essential to tolerate repeated hydrogen absorption–desorption cycles, which induce volumetric expansion and local lattice distortion. Insufficient stiffness may lead to structural degradation, while excessively rigid lattices can hinder hydrogen diffusion and release kinetics. The mechanical stability of cubic Mg_3ZH_8 (Z = Fe, Co) hydrides was evaluated using the Born–Huang stability criteria,[41] expressed as $C_{11} - C_{12} > 0$, $C_{44} > 0$, $C_{11} > 0$, and $C_{11} + 2C_{12} > 0$. The calculated elastic constants summarized in Table 3 satisfy all stability conditions, confirming that both Mg_3FeH_8 and Mg_3CoH_8 are mechanically stable.

Table 3 indicates Mg_3FeH_8 exhibits significantly higher stiffness than Mg_3CoH_8, with C_{11} = 296.53 GPa and C_{12} = 150.80 GPa,

Table 3 Calculated elastic constants (C_{ij}, in GPa), polycrystalline elastic moduli (B, G, E in GPa), and elastic anisotropy indices (A, A^B, A^G, A^U) of Mg_3ZH_8 (Z = Fe, Co)

	Elastic constants			Elastic moduli			Elastic anisotropy indices			
Compound	C_{11}	C_{12}	C_{44}	B	G	E	A	A^B	A^G	A^U
Mg_3FeH_8	296.53	150.80	58.22	199.38	63.69	172.69	0.799	0.000	0.006	0.061
Mg_3CoH_8	182.34	49.57	36.01	93.82	46.12	118.87	0.542	0.000	0.044	0.463
Mg_7TiH_{16} (ref. 44)	125.81	18.55	16.33	82.31	31.45	84.27	—	—	—	—
Mg_7FeH_{16} (ref. 44)	137.92	28.3	22.71	89.76	35.82	95.41	—	—	—	—
K_2LiAlH_6 (ref. 34)	60.2	18.5	19.2	32.18	13.98	37.86	—	—	—	—
$LiCaCoH_6$ (ref. 45)	107.02	29.05	39.12	67.54	39.12	101.02	—	—	—	—
K_2LiTiH_6 (ref. 46)	43.68	18.12	28.18	26.84	17.89	45.76	—	—	—	—
Ca_2LiTiH_6 (ref. 46)	108.83	23.40	34.92	71.63	35.44	92.13	—	—	—	—

compared to C_{11} = 182.34 GPa and C_{12} = 49.57 GPa for Mg_3CoH_8. This indicates a much stronger resistance to longitudinal compression in the Fe-based lattice. The shear response follows the same trend, with C_{44} = 58.22 GPa for Mg_3FeH_8 and 36.01 GPa for Mg_3CoH_8, suggesting greater tolerance against shape distortions during hydrogen insertion and removal. Furthermore, the tetragonal shear parameter,[42] $C' = \frac{C_{11} - C_{12}}{2}$, is positive for both compounds ($\approx$72.87 GPa for Mg_3FeH_8 and $\approx$66.39 GPa for Mg_3CoH_8), confirming stability against shear-driven lattice instabilities.

As there are no previously reported experimental or theoretical elastic data for Mg_3ZH_8 (Z = Fe, Co) hydrides, a comparison with other complex and double-perovskite hydrides is provided in Table 3. Reported A_2BH_6-type and double-perovskite hydrides typically exhibit moderate stiffness, with C_{11} values in the range of ~44–138 GPa (*e.g.*, K_2LiAlH_6, $LiCaCoH_6$, Mg_7TiH_{16}-based systems). In contrast, Mg_3ZH_8 (Z = Fe, Co) shows substantially higher elastic stiffness, with C_{11} reaching nearly 300 GPa for Mg_3FeH_8, indicating an unusually rigid hydrogen-rich framework. This distinct combination of high elastic resilience and high hydrogen content differentiates Mg_3ZH_8 (Z = Fe, Co) from previously reported complex and perovskite hydrides,[34,43–45] underscoring its scientific novelty and suitability for durable solid-state hydrogen storage under repeated cycling conditions.

The elastic response of Mg_3ZH_8 (Z = Fe, Co) is closely linked to its lattice vibrational behavior, providing a direct connection between mechanical stiffness and phonon dynamics. Higher elastic constants, particularly C_{11} and C_{44}, correspond to increased sound velocities and stiffer acoustic phonon branches, which enhance lattice stability and suppress low-frequency soft modes. In Mg_3FeH_8, the larger elastic stiffness is therefore consistent with its wider acoustic–optical phonon separation and the absence of imaginary frequencies in the phonon dispersion (Fig. 1(a)), confirming robust dynamical stability. Conversely, the comparatively lower elastic constants of Mg_3CoH_8 lead to softer acoustic phonons, which facilitate lattice flexibility and hydrogen-induced vibrational motion during absorption and desorption (Fig. 1(b)).

Elastic anisotropy describes the directional dependence of mechanical response, which is highly relevant for hydrogen-rich solids because hydrogen uptake and release generate directional lattice strain and non-uniform stress fields. In practical hydrogen storage, anisotropy affects microcrack initiation, diffusion pathways, and long-term cycling durability. In this work, the anisotropic behavior of Mg_3ZH_8 (Z = Fe, Co) is evaluated using the Zener anisotropy index $\left(A = \frac{2C_{44}}{C_{11} - C_{12}}\right)$, the bulk and shear anisotropy indices $\left(A^B = \frac{B_V - B_R}{B_V + B_R},\ A^G = \frac{G_V - G_R}{2G_H}\right)$, and the universal anisotropy index $\left(A^U = 5\frac{G_V}{G_R} + \frac{B_V}{B_R} - 6\right)$.[46] For cubic systems, isotropy is indicated by A = 1, while $A^B = A^G = A^U = 0$ corresponds to fully isotropic behavior.[46] For Mg_3FeH_8, the Zener anisotropy index is A = 0.799, which deviates from unity and therefore confirms elastic anisotropy. Mg_3CoH_8 shows a stronger deviation with A = 0.542, indicating that the Co-based hydride is more anisotropic than the Fe-based phase. This trend is consistent with their elastic constants: Mg_3CoH_8 has a much smaller C_{12} relative to C_{11}, which increases the directional contrast between shear and longitudinal deformation and enhances anisotropy. The tetragonal shear stability parameter C' remains positive, confirming that the anisotropy does not arise from instability but from intrinsic bonding asymmetry within the H-rich framework. The bulk anisotropy index is essentially zero for both materials ($A^B \approx 0.000$), indicating that the compressibility is nearly isotropic. This is beneficial for hydrogen storage because volumetric expansion during hydrogen loading is less likely to concentrate stress along a single axis, reducing the probability of catastrophic lattice failure. In contrast, the shear anisotropy index shows a clear difference: Mg_3FeH_8 exhibits a very small value (A^G = 0.006), while Mg_3CoH_8 has a much larger shear anisotropy (A^G = 0.044). The same conclusion is supported by the universal anisotropy index, which is low for Mg_3FeH_8 (A^U = 0.061) but significantly higher for Mg_3CoH_8 (A^U = 0.463). These results indicate that Mg_3FeH_8 is closer to isotropic mechanical behavior, whereas Mg_3CoH_8 exhibits stronger directional sensitivity, mainly governed by shear deformation.

To connect single-crystal stiffness to polycrystalline mechanical performance, the Voigt and Reuss bounds for the bulk and shear moduli were evaluated and subsequently averaged using the Voigt–Reuss–Hill (VRH) scheme. For cubic symmetry, the moduli are given by:[24,25]

$$B_V = \frac{1}{3}(C_{11} + 2C_{12}),\ \text{and}\ G_V = \frac{1}{5}(C_{11} - C_{12} + 3C_{44}) \quad (1)$$

$$B_R = \frac{1}{3}(C_{11} + 2C_{12}),\ \text{and}\ G_R = \frac{5C_{44}(C_{11} - C_{12})}{4C_{44} + 3(C_{11} - C_{12})} \quad (2)$$

The Hill averages were obtained as

$$B = \frac{1}{2}(B_V + B_R),\ \text{and}\ G = \frac{1}{2}(G_V + G_R) \quad (3)$$

and Young's modulus and Poisson's ratio were determined from

$$E = \frac{9BG}{3B + G},\ \text{and}\ \nu = \frac{(3B - 2G)}{2(3B + G)} \quad (4)$$

The calculated elastic moduli listed in Table 3 are consistent with those reported for comparable complex hydrides, confirming the reliability of the present calculations.[34,43–45]

The bulk modulus B reflects resistance to volumetric compression and is directly relevant to lattice stability during hydrogen uptake. Mg_3FeH_8 exhibits a high bulk modulus (B = 199.38 GPa), which is significantly larger than those reported for typical complex hydrides such as Mg_7TiH_{16} (~82 GPa),[43] Mg_7FeH_{16} (~90 GPa),[43] and K_2LiAlH_6 (~32 GPa),[34] indicating strong resistance to hydrogen-induced lattice expansion and favorable cycling stability. Mg_3CoH_8 shows a moderate bulk modulus (B = 93.82 GPa), comparable to Mg_7FeH_{16},[43] and $LiCaCoH_6$,[44] suggesting a more compliant lattice that may

facilitate hydrogen diffusion while maintaining mechanical integrity.

The shear modulus G governs resistance to shape deformation and plays a key role in suppressing lattice distortion and crack formation during cycling. Mg_3FeH_8 exhibits a higher shear modulus (G = 63.69 GPa) than Mg_3CoH_8 (G = 46.12 GPa), and exceeds values reported for Mg_7TiH_{16} (~31 GPa)[43] and K_2LiAlH_6 (~14 GPa).[34] This enhanced shear resistance supports greater mechanical durability in the Fe-based hydride, while the lower G of Mg_3CoH_8 may facilitate lattice flexibility favorable for hydrogen diffusion.

Young's modulus E, which characterizes overall elastic stiffness, follows the same trend. Mg_3FeH_8 shows a high Young's modulus (E = 172.69 GPa), substantially exceeding those of Mg_7TiH_{16} (~84 GPa),[43] Mg_7FeH_{16} (~95 GPa),[43] and K_2LiAlH_6 (~38 GPa).[34] Mg_3CoH_8 exhibits a moderate value (E = 118.87 GPa), still higher than most reported complex hydrides. Collectively, these comparisons indicate that Mg_3ZH_8 (Z = Fe, Co) combines high elastic stiffness with hydrogen-rich chemistry, highlighting its mechanical robustness and reinforcing the reliability of the VRH-based elastic analysis.

Poisson's ratio (ν), Pugh's ratio (B/G), and Cauchy pressure ($C_P = C_{12} - C_{44}$) provide insight into bonding character, ductility, and mechanical adaptability, all of which directly influence hydrogen cycling durability. In general, ν values near 0.33 indicate metallic bonding, values around 0.25 suggest ionic bonding, and values near 0.1 are characteristic of covalent bonding, while $\nu > 0.26$ and $B/G > 1.75$ are commonly associated with ductile behavior.[47,48] Positive Cauchy pressure further reflects ionic bonding and enhanced plasticity, whereas negative values indicate covalent bonding and brittleness.[49] The mechanical indicators are listed in Table 4 further clarify the ductility, bonding character, and hydrogen-cycling resilience of Mg_3ZH_8 (Z = Fe, Co). The Cauchy pressure (C_P) is positive for both compounds, confirming dominant metallic bonding. However, Mg_3FeH_8 exhibits a markedly larger value (92.58 GPa) than Mg_3CoH_8 (13.56 GPa), indicating superior ductility and resistance to hydrogen-induced embrittlement. This enhanced ductility is also reflected in the Pugh's ratio (B/G), where Mg_3FeH_8 (B/G = 3.13) and Mg_3CoH_8 (B/G = 2.03) both exceed the brittle–ductile threshold (≈1.75), with the Fe-based hydride showing a stronger ductile character. These results suggesting enhanced mechanical resilience during repeated hydrogen absorption–desorption cycles. The Poisson's ratio (ν) further supports this trend, with values of 0.356 for Mg_3FeH_8 and 0.289 for Mg_3CoH_8, consistent with metallic bonding and good plastic deformability during repeated hydrogen absorption–desorption cycles. The Vickers hardness[50] (H_V), estimated using $H_V = (1 - 2\nu)Y/[6(1 + \nu)]$, quantifies resistance to plastic deformation and is therefore directly relevant to hydrogen cycling durability. Despite differences in ductility, both compounds exhibit comparable Vickers hardness ($H_V \approx$ 6–6.5 GPa), suggesting sufficient resistance to surface deformation without excessive brittleness.

The calculated hardness values of Mg_3FeH_8 and Mg_3CoH_8 (≈6–6.5 GPa) are comparable to those reported for Mg_3CrH_8 (6.21 GPa) and Mg_3MnH_8 (5.37 GPa), and slightly higher than Mg_3TiH_8 and Mg_3VH_8, as reported in the literature.[19] This indicates that the Fe- and Co-based hydrides possess sufficient resistance to surface deformation while retaining ductile characteristics, which is favorable for suppressing crack formation and mechanical degradation during hydrogen cycling.

When compared with other hydride perovskites such as $MgCuH_3$ (0.77 GPa),[51] $RbNiH_3$ (0.64 GPa),[52] $BeGaH_3$ (3.02 GPa),[53] and $BeInH_3$ (3.17 GPa),[53] both Mg_3FeH_8 and Mg_3CoH_8 exhibit relatively high hardness values, confirming their favorable mechanical stability among hydrogen-rich hydrides. The machinability index $\left(\mu_M = \frac{B}{C_{44}}\right)$ provides insight into both intrinsic plasticity and industrial workability.[54] Finally, the higher machinability index (μ_m = 3.42) of Mg_3FeH_8 compared to Mg_3CoH_8 (2.61) implies improved processability and structural tolerance, which are advantageous for fabricating durable hydrogen storage components. Collectively, these parameters demonstrate that Mg_3ZH_8 (Z = Fe, Co) hydrides combine metallic ductility with mechanical robustness, reinforcing their suitability for stable and kinetically efficient solid-state hydrogen storage.

The Debye temperature (Θ_D) is a key thermophysical parameter that governs lattice vibrational behavior, heat capacity, lattice stability, and thermal conductivity, all of which are directly relevant to hydrogen storage kinetics and reversibility. In solid-state hydrides, Θ_D reflects the strength of interatomic bonding and the ability of the lattice to withstand repeated hydrogen absorption–desorption cycles without structural degradation. A higher Θ_D generally indicates stronger metal–hydrogen bonding and enhanced lattice stability, while moderate reductions in Θ_D can facilitate hydrogen diffusion and release. The Debye temperature was calculated using the following relations:[55]

$$\Theta_D = \frac{h}{k_B}\left[\frac{3n}{4\pi V_0}\right]^{1/3} v_m \quad (5)$$

$$v_m = \left[\frac{1}{3}\left(\frac{2}{v_t^3} + \frac{1}{v_l^3}\right)\right]^{-\frac{1}{3}},\ v_l = \left(\frac{B + \frac{3}{4}G}{\rho}\right) \text{ and } v_t = \left[\frac{G}{\rho}\right]^{\frac{1}{2}} \quad (6)$$

Table 4 Ductility indicators (C_P, ν, B/G), machinability (μ_m), density (ρ in kg m^{-3}), sound velocities (v_t, v_l, v_m in km s^{-1}), Debye and melting temperatures (θ_D, T_m in K), lattice and minimum thermal conductivities (k_{ph}, k_{min} in W m^{-1} K^{-1}) of Mg_3ZH_8 (Z = Fe, Co)

Compound	C_P	B/G	ν	H_V	μ_m	ρ	v_t	v_l	v_m	θ_D	T_m	k_{ph}	k_{min}
Mg_3FeH_8	92.58	3.13	0.356	6.13	3.42	5.89	3.29	6.05	3.70	746.4	2305	3.39	2.35
Mg_3CoH_8	13.56	2.03	0.289	6.49	2.61	5.76	2.83	5.19	3.16	627.3	1631	3.57	1.94

where v_l and v_t are the longitudinal and transverse sound velocities, B and G are the bulk and shear moduli, ρ is the density, n is the number of atoms per unit cell, and V_0 is the unit-cell volume.

As summarized in Table 4, Mg_3FeH_8 exhibits higher sound velocities and a larger average phonon velocity than Mg_3CoH_8. Consequently, Mg_3FeH_8 shows a higher Debye temperature (Θ_D = 746.4 K) compared to Mg_3CoH_8 (Θ_D = 627.3 K), indicating stronger interatomic bonding and enhanced lattice rigidity. When compared with previously reported single, complex, and double hydrides, the thermo-mechanical characteristics of Mg_3FeH_8 and Mg_3CoH_8 fall within a favorable range for durable hydrogen storage. Typical single perovskite hydrides such as $MgXH_3$ (X = Ga, Tl),[29] $MgCuH_3$,[56] $MBeH_3$ (M = Li, Na, and K),[57] and $XFeH_3$ (X = Ca, Sr, Ba)[58] exhibit Debye temperatures generally below ~400 K, reflecting softer lattices that are more susceptible to hydrogen-induced vibrational instability during cycling. In contrast, several complex and double hydrides, including Cs_2NaInH_6,[59] Sr_2LiCuH_6,[11] and $BaXH_4$ (X = Mn, Re, or Tc)[60] display Debye temperatures in the range of 300–550 K, indicating improved lattice stiffness and phonon stability. The Debye temperatures of Mg_3FeH_8 and Mg_3CoH_8 are comparable to or higher than those of many established similar type hydrides,[19] suggesting similarly robust vibrational stability under repeated hydrogen absorption–desorption cycles. This insight provides a rational design principle for developing thermally stable, high-capacity solid-state hydrogen storage materials suitable for stationary and high-temperature hydrogen energy applications. However, the absence of imaginary phonon modes, high Debye temperatures, ductile mechanical behavior, and moderate reaction enthalpies suggest favorable lattice resilience and potential hydrogen mobility.

The melting temperature (T_m) is a key indicator of mechanical robustness and thermal endurance, which are essential for solid-state hydrogen storage materials operating under repeated absorption–desorption cycles. A sufficiently high T_m ensures that the host lattice maintains its structural integrity at elevated temperatures required for hydrogen release, while also preventing mechanical degradation during long-term cycling. Consequently, T_m is closely linked to hydrogen storage kinetics, safety, and operational reliability. The melting temperature was estimated using the empirical relation:[61]

$$T_m = 553 + 5.91C_{11}\ (\pm 300\ \text{K}) \quad (7)$$

Using this relation, Mg_3FeH_8 exhibits a significantly higher melting temperature ($T_m \approx 2305$ K) compared to Mg_3CoH_8 ($T_m \approx 1631$ K). This difference directly correlates with their elastic stiffness, as Mg_3FeH_8 possesses a much larger C_{11} and bulk modulus than Mg_3CoH_8, indicating stronger interatomic bonding and greater resistance to lattice deformation. From a hydrogen storage perspective, the higher T_m of Mg_3FeH_8 implies superior thermal stability, making it suitable for high-temperature hydrogen storage and stationary energy systems, where structural durability is critical. In contrast, the lower T_m of Mg_3CoH_8 reflects a comparatively softer lattice, which can facilitate lattice breathing and atomic rearrangements during hydrogen desorption. Such behavior is advantageous for enhancing hydrogen release kinetics at reduced temperatures, highlighting a trade-off between thermal robustness and kinetic accessibility. A comparison with previously reported hydrides further clarifies the thermal robustness of Mg_3FeH_8 and Mg_3CoH_8. Single perovskite hydrides such as $MgCuH_3$,[56] $CsAH_3$ (A = Fe, Cu and Tl),[62] and $XFeH_3$ (X = Ca, Sr, Ba)[58] generally exhibit lower estimated melting temperatures, which limits their resistance to thermally induced lattice degradation during hydrogen cycling. In contrast, complex and double hydrides, including Cs_2NaInH_6,[59] Cs_2AlInH_6,[59] Cs_2AlTlH_6,[59] and X_2MgH_4 (X = K, Rb, Cs),[63] display moderate melting temperatures, reflecting improved thermal endurance and cycling stability. This combination of high melting temperature, strong mechanical stability, and hydrogen-rich composition highlights the scientific novelty of Mg_3ZH_8 (Z = Fe, Co) hydrides.

The lattice thermal conductivity (κ_{ph}) was evaluated using Slack's model, which correlates the Debye temperature, Grüneisen parameter (γ), and other lattice descriptors:[64]

$$\kappa_{ph} = A(\gamma)\frac{M_{av}\theta_D{}^3\delta}{\gamma^2 n^{2/3}T} \quad (8)$$

where M_{av} is the average atomic mass, δ is the volume per atom, n is the number of atoms per unit cell, and $A(\gamma)$ is a constant. The anharmonicity in lattice vibrations, which governs phonon–phonon scattering, is quantified by the Grüneisen parameter:[65]

$$\gamma = \frac{3(1+v)}{2(2-3v)} \quad (9)$$

In addition, the minimum lattice thermal conductivity (k_{min}) was estimated using Clarke's model:[65]

$$k_{min} = k_B v_a \left(\frac{M}{n\rho N_A}\right)^{-2/3} \quad (10)$$

The calculated κ_{ph} and k_{min} values listed in Table 4 indicate that both Mg_3FeH_8 and Mg_3CoH_8 hydrides possess moderate phonon heat transport at 300 K. Mg_3FeH_8 shows κ_{ph} = 3.39 W m^{-1} K^{-1} and k_{min} = 2.35 W m^{-1} K^{-1}, whereas Mg_3CoH_8 exhibits a slightly higher κ_{ph} = 3.57 W m^{-1} K^{-1} but a lower k_{min} = 1.94 W m^{-1} K^{-1}. The larger k_{min} in Mg_3FeH_8 is consistent with its higher sound velocities and stronger lattice stiffness, implying a higher intrinsic phonon transport floor, while the comparatively lower k_{min} of Mg_3CoH_8 reflects a softer lattice that can enhance phonon scattering. From a hydrogen-storage perspective, these thermal transport characteristics are beneficial because efficient heat dissipation can mitigate local temperature gradients during absorption–desorption cycling, supporting stable kinetics and improved cycling durability.

4. Conclusion

First-principles calculations provide a powerful framework for the discovery and rational design of advanced hydrogen storage materials. In this study, transition-metal substitution into magnesium-based hydrides was explored as an effective strategy to tailor hydrogen storage thermodynamics and kinetics. The structural, electronic, mechanical, optical, and hydrogen storage properties of Mg_3ZH_8 (Z = Fe, Co) were systematically investigated using density functional theory to assess their suitability for solid-state hydrogen storage applications. Both compounds are found to be thermodynamically, mechanically, and dynamically stable, as confirmed by negative formation energies, elastic stability criteria, and phonon spectra free of imaginary modes. Mg_3FeH_8 exhibits a ferromagnetic metallic ground state, whereas Mg_3CoH_8 is non-magnetic, highlighting the role of transition-metal d states in governing magnetic and electronic behavior. The hydrogen storage performance of Mg_3ZH_8 (Z = Fe, Co) is promising, with gravimetric capacities of 5.90 wt% for Mg_3FeH_8 and 5.76 wt% for Mg_3CoH_8, exceeding the U.S. DOE minimum target. Their volumetric hydrogen densities ($\approx$195–187 g H_2 per L) are substantially higher than current DOE benchmarks, indicating excellent space efficiency. The calculated desorption temperatures fall within a moderate range, with Mg_3FeH_8 consistently showing lower T_{des} values than Mg_3CoH_8, suggesting more favorable hydrogen release kinetics. Mechanical analysis reveals that both hydrides are ductile, with positive Cauchy pressures, high Pugh's ratios, and moderate Vickers hardness values, implying good resistance to hydrogen-induced embrittlement during cycling. Optical and electronic analyses further confirm their metallic nature, with strong free-carrier response and interband transitions that correlate with their hydrogen desorption behavior. Overall, the balanced combination of high hydrogen density, mechanical resilience, moderate desorption temperature, and electronic activity positions Mg_3ZH_8 (Z = Fe, Co), particularly Mg_3FeH_8, as a promising candidate for next-generation hydrogen storage materials and provides a robust theoretical benchmark for future experimental exploration.

Author contributions

Md. Hasan Mia: conceptualization; methodology; writing manuscript – reviewing and editing; data curation; validation; supervision; Md. Zahid Hasan: formal analysis; validation; review – editing. A. Arunkumar: formal analysis; validation; review – editing; and supervision. S. AlFaify: formal analysis; validation; review – editing.

Conflicts of interest

The authors declare that they have no known conflicting financial interests or personal ties that may have seemed to affect the work presented in this study.

Data availability

Supplementary information: the figures in the supplementary information represent the optical conductivity and refractive properties of Mg_3ZH_8 (Z = Fe, Co) hydrides. See DOI: https://doi.org/10.1039/d6ma00353b.

Relevant data from this study are available from the corresponding author upon a reasonable request.

Acknowledgements

The authors are grateful to the Materials Research and Simulation lab, Department of Electrical Electronics and Engineering, International Islamic University Chittagong, Chittagong-4358, Bangladesh for providing the computing facilities for this work.

References

1 L. Zhou, *Renewable Sustainable Energy Rev.*, 2005, **9**, 395–408.
2 E. Fakioğlu, Y. Yürüm and T. N. Veziroğlu, *Int. J. Hydrogen Energy*, 2004, **29**, 1371–1376.
3 S. Niaz, T. Manzoor and A. H. Pandith, *Renewable Sustainable Energy Rev.*, 2015, **50**, 457–469.
4 V. Kudiiarov, J. Lyu, O. Semyonov, A. Lider, S. Chaemchuen and F. Verpoort, *Appl. Mater. Today*, 2021, **25**, 101208.
5 R. Zhou, X. Mo, Y. Huang, C. Hu, X. Zuo, Y. Ma, Q. Wei and W. Jiang, *Batteries*, 2023, **9**, 179.
6 J. Zheng, W. Sun, X. Dou, A.-J. Mao and C. Lu, *J. Phys. Chem. C*, 2021, **125**, 3150–3156.
7 Y. Ma, D. Duan, Z. Shao, H. Yu, H. Liu, F. Tian, X. Huang, D. Li, B. Liu and T. Cui, *Phys. Rev. B:Condens. Matter Mater. Phys.*, 2017, **96**, 144518.
8 T. Tang and Y. Tang, *Int. J. Hydrogen Energy*, 2024, **61**, 13–24.
9 A. Hosen, D. Dahliah, N. F. AlShaikh Mohammad, A. A. Mousa and M. S. Abu-Jafar, *Int. J. Hydrogen Energy*, 2025, **102**, 348–359.
10 G. M. Mustafa, B. Younas, H. D. Alkhaldi, A. Mera, A. K. Alqorashi, J. Hakami, S. A. Mahmoud, I. Boukhris and Q. Mahmood, *Int. J. Hydrogen Energy*, 2024, **95**, 300–308.
11 A. Ayyaz, M. A. Ullah, M. Zaman, N. D. Alkhaldi, Q. Mahmood, I. Boukhris, M. S. Al-Buriahi and M. M. Al-Anazy, *Int. J. Hydrogen Energy*, 2025, **102**, 1329–1339.
12 W. Azeem, S. Hussain, M. K. Shahzad, F. Azad, G. Khan, V. Tirth, H. Alqahtani, A. Algahtani, T. Al-Mughanam and Y. H. Wong, *Int. J. Hydrogen Energy*, 2024, **79**, 514–524.
13 Q. Dai, T.-Y. Tang, Q.-Q. Liang, Z.-Q. Chen, Y. Wang and Y.-L. Tang, *Int. J. Hydrogen Energy*, 2024, **92**, 769–778.
14 T. Tang and Y. Tang, *Mater. Chem. Phys.*, 2024, **316**, 129099.
15 Y. Pan and Y. Zhu, *J. Alloys Compd.*, 2025, **1021**, 179661.
16 H. Murtaza, Q. Ain, R. A. Alshgari, T. Akhter and J. Munir, *J. Power Sources*, 2025, **641**, 236788.
17 D. Tufail, U. Ahmed, M. Haleem, B. Amin and M. Shafiq, *RSC Adv.*, 2025, **15**, 337–347.
18 M. M. Al-Anazy, G. M. Mustafa, O. Zayed, B. Younas, T. M. Al-Daraghmeh, N. D. Alkhaldi, A. S. Alofi,

A. K. Alqorashi and Q. Mahmood, *Int. J. Hydrogen Energy*, 2024, **78**, 927–937.
19 T. Tang and Y. Tang, *Int. J. Hydrogen Energy*, 2024, **74**, 372–383.
20 M. D. Segall, P. J. D. Lindan, M. J. Probert, C. J. Pickard, P. J. Hasnip, S. J. Clark and M. C. Payne, *J. Phys.: Condens. Matter*, 2002, **14**, 2717.
21 J. P. Perdew, K. Burke and M. Ernzerhof, *Phys. Rev. Lett.*, 1996, **77**, 3865.
22 P. E. Gill, W. Murray and M. A. Saunders, *SIAM Rev.*, 2005, **47**, 99–131.
23 P. Wisesa, K. A. McGill and T. Mueller, *Phys. Rev. B:Condens. Matter Mater. Phys.*, 2016, **93**, 155109.
24 W. Voigt, *Lehrbuch der Kristallphysik (Textbook of crystal physics)*, BG Teubner, Leipzig und Berlin, 1928.
25 A. Reuß, *Z. Angew. Math. Mech.*, 1929, **9**, 49–58.
26 M. Bortz, B. Bertheville, K. Yvon, E. A. Movlaev, V. N. Verbetsky and F. Fauth, *J. Alloys Compd.*, 1998, 279.
27 L. Yi, *Trans. Nonferrous Met. Soc. China*, 2010, **20**, 2281–2288.
28 E. Evard, I. Gabis and V. A. Yartys, *Int. J. Hydrogen Energy*, 2010, **35**, 9060–9069.
29 M. H. Mia, M. S. Parves, O. Alsalmi and M. Z. Hasan, *ACS Appl. Eng. Mater.*, 2025, **3**, 4218–4232.
30 S. Al, *Int. J. Hydrogen Energy*, 2019, **44**, 1727–1734.
31 T. Tang and Y. Tang, *Ceram. Int.*, 2024, **50**, 52270–52283.
32 S. Zhang, S. Chen, Y. Chen, J. Hou, D. Xu, W. Luo and Z. Shi, *Int. J. Hydrogen Energy*, 2025, **166**, 150903.
33 Z. El Fatouaki, A. Tahiri, A. Jabar and M. Idiri, *Int. J. Hydrogen Energy*, 2025, **175**, 151433.
34 H. Murtaza, M. A. Habib, Q. Ain, A. Kumar, J. Munir, A. B. M. Ibrahim, A. D. Oza and M. S. S. Al-Salimi, *Sci. Rep.*, 2025, **16**, 2019.
35 M. Caid, E. Deligöz, H. Ozisik, H. Rached, D. Rached, H. Mansour and Y. Rached, *Int. J. Hydrogen Energy*, 2025, **182**, 151797.
36 T. Ikeda, Y. Mikami and T. Haruki, *J. Phys. Chem. C*, 2007, **111**, 8389–8396.
37 Y. Didi, A. Tahiri, R. Touti, R. Ahfir, M. Naji, H. Naïli, H. Nebdi, C. Hajjaj and A. Rjeb, *Int. J. Hydrogen Energy*, 2026, **225**, 154319.
38 M. W. Qureshi, X. Ma, G. Tang and R. Paudel, *Materials*, 2020, **13**, 5148.
39 M. H. Mia, M. A. Khatun and M. Rahman, *Next Mater.*, 2025, **7**, 100434.
40 V. Lucarini, K. E. Peiponen, J. J. Saarinen and E. M. Vartiainen, *Kramers-Kronig relations in optical materials research*, Springer Berlin Heidelberg, Berlin, Heidelberg, 2005, vol. 110, pp. 27–28.
41 F. Mouhat and F.-X. Coudert, *Phys. Rev. B:Condens. Matter Mater. Phys.*, 2014, **90**, 224104.
42 M. H. Mia, F. Parvin, A. K. M. A. Islam and M. A. Khatun, *Int. J. Mod. Phys. B*, 2025, **39**, 2550118.
43 S. Berri and Ç. Yamçıçıer, *Int. J. Hydrogen Energy*, 2025, **177**, 151559.
44 A. Hosen, E. N. Kande, H. D. Alkhaldi, A. A. Mousa, A. Akremi, I. Boukhris and M. S. Abu-Jafar, *J. Mater. Res. Technol.*, 2025, **36**, 8688–8697.
45 M. A. Ullah, M. Kaleem, A. Nasir, Z. Sarfraz, M. M. A. Iqbal, M. Rizwan, K. N. Riaz and M. Tanzeel, *RSC Adv.*, 2025, **15**, 38714–38728.
46 J. K. Rony, M. Islam, M. Saiduzzaman, K. M. Hossain, S. Alam, A. Biswas, M. H. Mia, S. Ahmad and S. K. Mitro, *J. Mater. Res. Technol.*, 2024, **29**, 897–909.
47 I. N. Frantsevich, *Elastic Constants and Elastic Moduli of Metals and Insulators*, 1982.
48 S. F. Pugh, *Philos. Mag.*, 1954, **45**, 823–843.
49 D. G. Pettifor, *Mater. Sci. Technol.*, 1992, **8**, 345–349.
50 Y. Tian, B. Xu and Z. Zhao, *Int. J. Refract. Met. Hard Mater.*, 2012, **33**, 93–106.
51 Z. U. Rehman, M. A. Rehman, B. Rehman, S. Sikiru, S. Qureshi, E. M. Ali and M. Awais, *Environ. Sci. Pollut. Res.*, 2023, **30**, 113889–113902.
52 W. Khan and M. K. Masood, *Mater. Sci. Semicond. Process.*, 2024, **173**, 108149.
53 W. Khan, *Mater. Sci. Semicond. Process.*, 2024, **174**, 108221.
54 Z. Sun, D. Music, R. Ahuja and J. M. Schneider, *Phys. Rev. B:Condens. Matter Mater. Phys.*, 2005, **71**, 193402.
55 P. Debye, *Ann. Phys.*, 1912, **344**, 789–839.
56 A. Koufi, Y. Ziat, H. Belkhanchi and A. Bouzaid, *Comput. Condens. Matter*, 2025, e01010.
57 D. Guendouz, Z. Charifi, H. Baaziz, T. Ghellab, N. Arikan, Ş. Uğur and G. Ö. K. A. Y. Uğur, *Can. J. Phys.*, 2016, **94**, 865–876.
58 R. Song, N. Xu, Y. Chen, S. Chen, J. Zhang, W. Dai and W. Zhang, *Chin. J. Phys.*, 2024, **89**, 1152–1163.
59 M. Tarekuzzaman, M. S. Parves, M. Z. Rahman and S. S. Hasan, *Solid State Commun.*, 2025, 116043.
60 E. Ededet, H. Louis, U. G. Chukwu, T. O. Magu, A. E. Udo, S. A. Adalikwu and A. S. Adeyinka, *J. Electron. Mater.*, 2024, 53.
61 M. E. Fine, L. D. Brown and H. L. Marcus, *Scr. Metall.*, 1984, **18**, 951–956.
62 M. H. Mia, M. Rasheduzzaman, O. Alsalmi and M. Z. Hasan, *Int. J. Hydrogen Energy*, 2026, **209**, 153607.
63 Ç. Yamçıçıer, *Int. J. Hydrogen Energy*, 2023, **48**, 39930–39943.
64 D. T. Morelli and G. A. Slack, *High Thermal Conductivity Materials*, Springer, New York, 2006, pp. 37–68.
65 D. R. Clarke, *Surf. Coat. Technol.*, 2003, **163**, 67–74.